Spectral Dependence of Direct and Trap-Mediated Recombination Processes in Lead Halide Perovskites using Time Resolved Microwave Conductivity: SUPPLEMENTARY MATERIAL

Joanna A. Guse, Arman M. Soufiani, Liangcong Jiang, Jincheol Kim, Yi-Bing Cheng, Timothy W. Schmidt, Anita Ho-Baillie, and Dane R. McCamey*

(Dated: March 2, 2016)

S1: KINETIC MODEL

The charge carrier dynamics in intrinsic, organo-lead halide perovskites upon photo-excitation can be described using the kinetic model described in Figure 1.

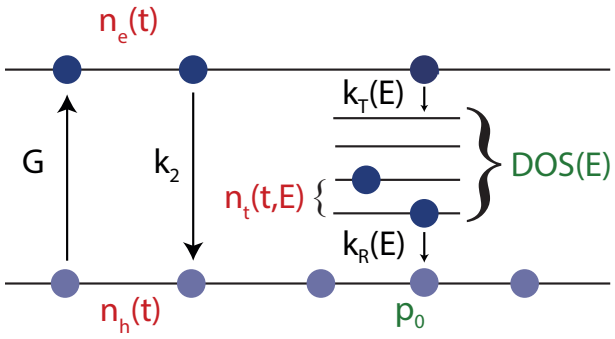

FIG. 1: Model of opto-electronic processes in organo-lead halide perovskites.

Consider a sample with a total trap density N_T and a population of holes p_0 present at thermal equilibrium, in either non-intrinsic perovskites or in intrinsic perovskites which are unintentionally doped. Upon illumination, immobile valence band electrons are excited into the conduction band, resulting in a photoinduced concentration of free electrons and holes, denoted n_e and n_h. The rate of photoexcitation G depends on both the laser excitation profile and the perovskite absorption kinetics at a given wavelength. Mobile electrons can recombine with holes directly at a rate k_2, or become immobilized in intra-band trapped states with a rate $k_T(E)$, giving rise to a population of trapped charges $n(t, E)$. This population of trapped charges is then able to recombine with holes at a rate of $k_R(E)$.

Hutter et al.[1] have considered the simplest case where k_T and k_R are constants which describe the average transition rate from the conduction band to a trapped state or from the trap state back to the valence band. We fit our data to this simple model, and find that it cannot accurately describe our data (see Fig: 2).

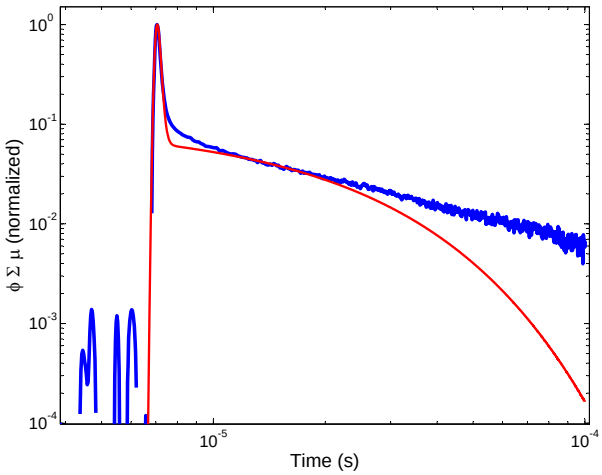

FIG. 2: TRMC trace fit by a simple model with constant trap transition rates k_T and k_R. This simple model[1] does not fit our data.

We suggest a modification to the model to take into account a continuous distribution of trapped states $P(E)$, which give rise to distributions of the decay rates.

The set of ODEs which describe the above model are:

$$\frac{dn_e}{dt} = G - k_2 n_e(n_h + p_0) - \left[n_e \int_{E_v}^{E_c} P(E)(N_T - n_t(E))k_T(E)dE \right]$$

$$\frac{dn_h}{dt} = G - k_2 n_e(n_h + p_0) - \left[(n_h - p_0) \int_{E_v}^{E_c} P(E)k_R(E)n_t(E)dE \right]$$

$$\frac{dn_t}{dt} = \left[n_e \int_{E_v}^{E_c} P(E)(N_T - n_t(E))k_T(E)dE \right] - \left[(n_h - p_0) \int_{E_v}^{E_c} P(E)k_R(E)n_t(E)dE \right],$$

where n_e, n_h and n_t are the time dependent concentrations of free electrons, free holes and trapped electrons respectively. N_T is the total density of charge traps, and p_0 denotes the equilibrium hole concentration before photoexcitation. k_2, $k_T(E)$ and $k_R(E)$ represent the electron-hole recombination rate, trap filling and trap emptying rates respectively.

S2: SAMPLE PREPARATION

$CH_3NH_3PbI_3$ films were deposited on clean thin (1 mm) high quality quartz substrates both at the University of New South Wales and Monash University using similar technique, namely gas-assisted technique [2]. In brief, 25 μL 45 wt% $CH_3NH_3PbI_3$ dimethylformamide (DMF) solution, prepared from PbI2 and CH3NH3I in a molar ratio of 1:1, was spread on the substrate, then spun at 6500 rpm. After 2 s a dry argon gas was blown on the solution during the spinning. Finally, the film was annealed at 100°C for 10 min to remove the residue solvent and induce crystallization. A thin layer of Poly(methyl methacrylate) (PMMA, Sigma-Aldrich) was coated on the top of the $CH_3NH_3PbI_3$ layer via spin coating at the speed of 2000 rpm in order to preserve the samples against air and moisture during the measurement.

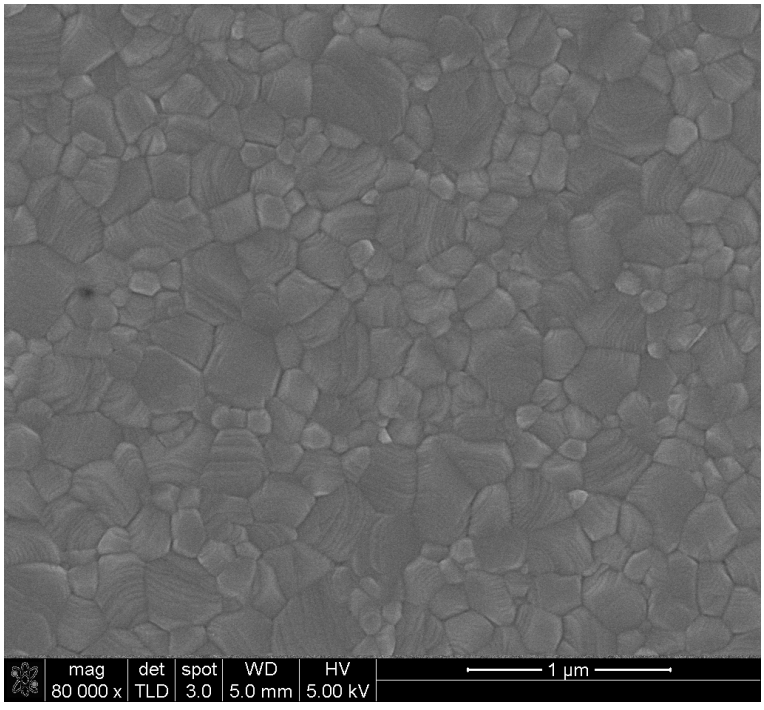

FIG. 3: SEM of $CH_3NH_3PbI_3$ sample. The grain size ranges from 100-300 nm.

S3: TRMC SETUP

There are three components which make up the TRMC detection setup: the laser excitation setup, the microwave cavity, and the microwave detection setup. The laser setup and cavity have been designed to allow for operation over a large range of excitation wavelengths and powers.

Laser excitation

An optical parametric oscillator (Opolette 355) was used as our tunable wavelength excitation source. The light was passed through a series of irises to eliminate cross beams, and was then passed through a linear polarizer to attenuate the polarization of the signal (or idler) component of the output light, which are nominally cross polarized. After the polarizer, neutral density filters were inserted while performing the intensity series for each wavelength. In this way, the power output of the laser could be measured once at high power where the thermal sensor (S401C) was most accurate, and then the intensity was back calculated from the filter transmission curve. The cross-over wavelength from the signal to idler in our OPO was at 710 nm, which meant that for wavelengths above 710 nm, an additional high pass filter was used to further attenuate leakage of the signal component of the laser output. A parabolic mirror fiber coupler was used to couple the light into a fiber and into the cavity. A calibration was performed to determine the power loss (vs wavelength) of the laser between the output of the fiber and the sample by unscrewing the cavity and placing the detector at the sample position.

Microwave Cavity

A custom built cavity is shown in Figure 4.

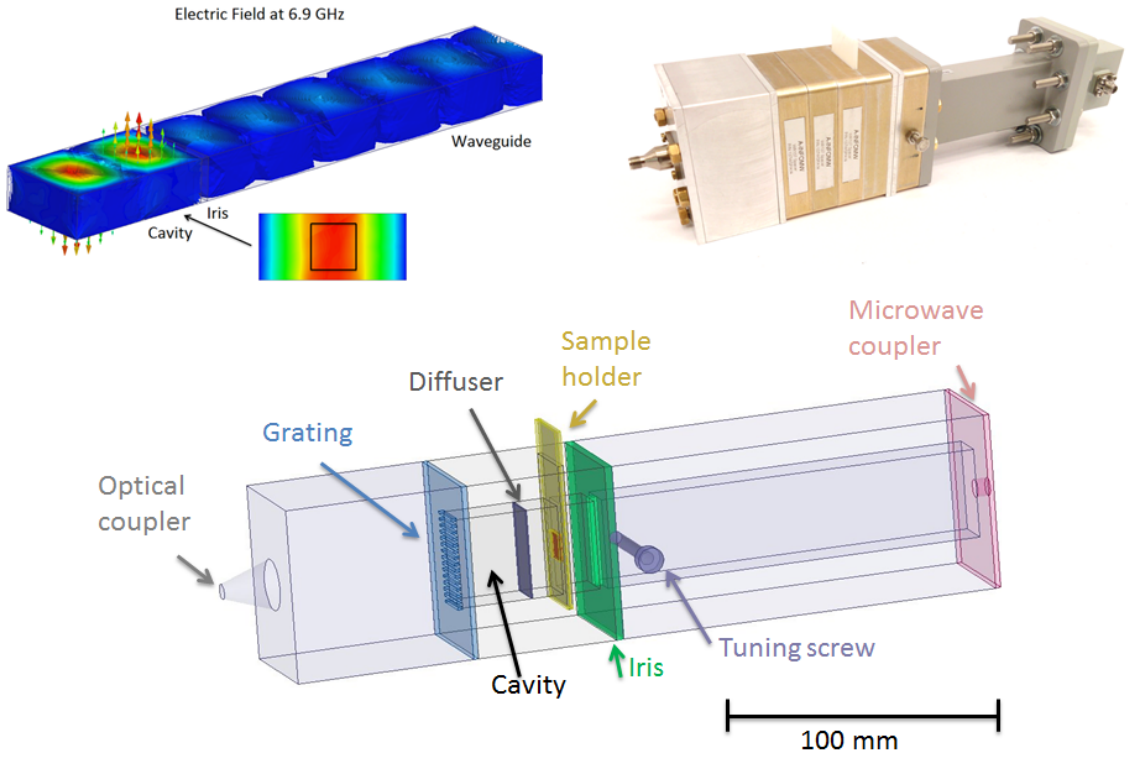

FIG. 4: Microwave cavity used for TRMC experiment. Top left: HFFS simulation of the electric field in the microwave cavity. The slice shows the electric field at the sample position. Top right: photo of the cavity. Bottom: model of the cavity.

Microwaves are coupled into the cavity (WR137) using an SMA connector. A slit iris is used to define one side of the cavity. A grating is used as a microwave short, while still allowing light to enter the cavity. An extra spacer is used to allow light input through an SMA terminated optical fiber to diverge until it fills the whole cavity area. A Teflon diffuser (placed at the node of the cavity) is used to diffuse the light in the cavity after it has passed the grating, such that the light incident on the sample is uniformly distributed. The sample is deposited on a 10×10 mm quartz substrate, which is held in place by two Teflon sample holders, with a cutout for the sample in the center. The sample holder is positioned at an anti-node of the cavity, where the electric field is maximum.

Complimentary microwave detection setups

We have developed two complimentary microwave detection setups: The first setup has a low noise floor, and measures power changes on a logarithmic scale, making it ideal for accurate measurements of the tail of the decay curves which has a small amplitude.

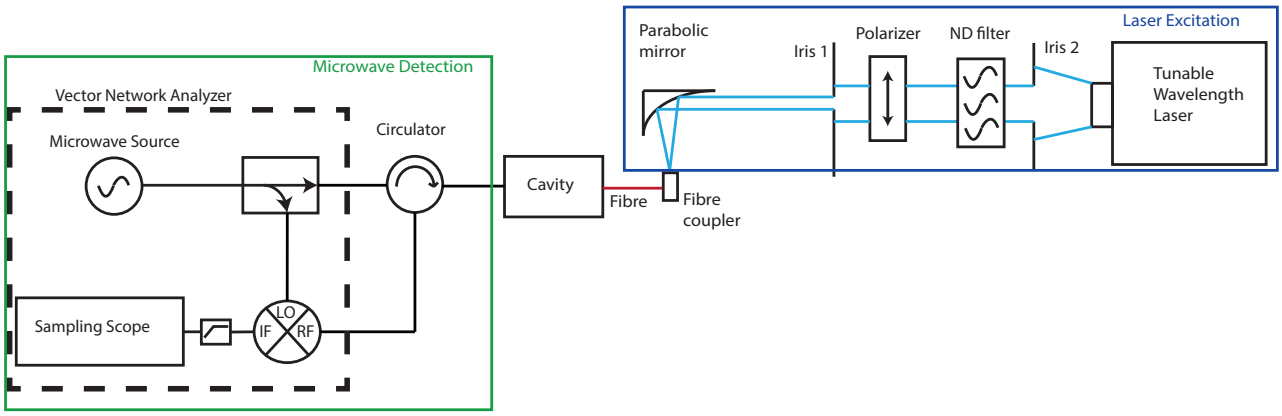

FIG. 5: DETECTION SETUP 1: This detection setup is optimized for its low noise floor, allowing for more accurate measurement of the long, small amplitude decay tail. The Fieldfox N9912A vector network analyzer was used as both the microwave source and also as a self contained detector, with a noise floor of about 0.1 dB, and an instrument response time of $\approx$ 70 ns.

The second setup is a handmade detection circuit which measures voltage changes on a linear scale, compromising it's noise floor for increased analog bandwidth.

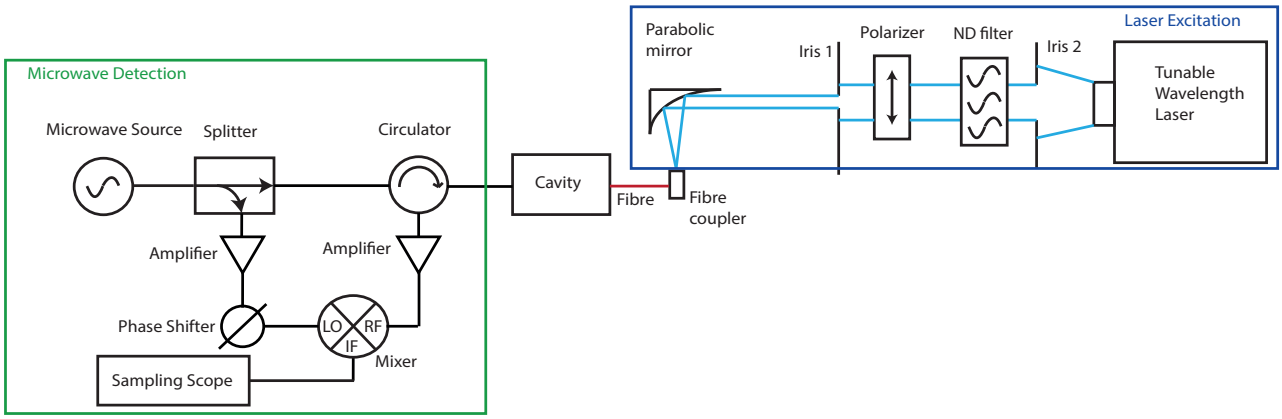

FIG. 6: DETECTION SETUP 2: This detection setup is optimized for its temporal response (response function is $<$ 1 ns).

In the second setup, a Fieldfox N9912A vector network analyzer was used as both the microwave source. A microwave splitter (minicircuits ZFRSC-123-S+) splits the microwave input into a signal and a reference arm. The reference arm passes through an amplifier (minicircuits ZX60-183A-S+) and a phase shifter (ARRA 9428A) before connecting to the local oscillator input of a mixed (minicircuits ZX05-14H-S+). the signal arm passes through a circulator (Fairview electronics SFC4080B), enters the microwave cavity, gets reflected back from the cavity, passes through the circulator into a signal amplifier (minicircuits ZX60-183A-S+) before being mixed with the reference signal. The resulting signal has components at the sum and difference frequencies of the inputs. The input on our oscilloscope (Agilent MSO9254A) acts as a high pass filter. The circuit response time is below 1 ns, and the risetime of our transient is limited by the laser risetime.

We use the second setup to confirm that our transients and resulting fits are not limited by the instrument response time in setup 1. All the data presented in our paper was taken with setup 1 to optimize the noise floor.

S4: POLARIZABILITY

We collected TRMC transients at various microwave frequencies across the cavity resonance ($f_0 = 6.5302$ GHz, $\Delta f = \pm 4$ MHz), using above (530 nm) and below (780 nm) bandgap excitation.

The cavity resonance can be reconstructed from the dark signal (average baseline), taken at various microwave frequencies across the resonance (red trace in figure 7). The frequency sweep should be chosen based on the Q factor of the cavity, so that the curve can be fit with a Gaussian/Lorentzian.

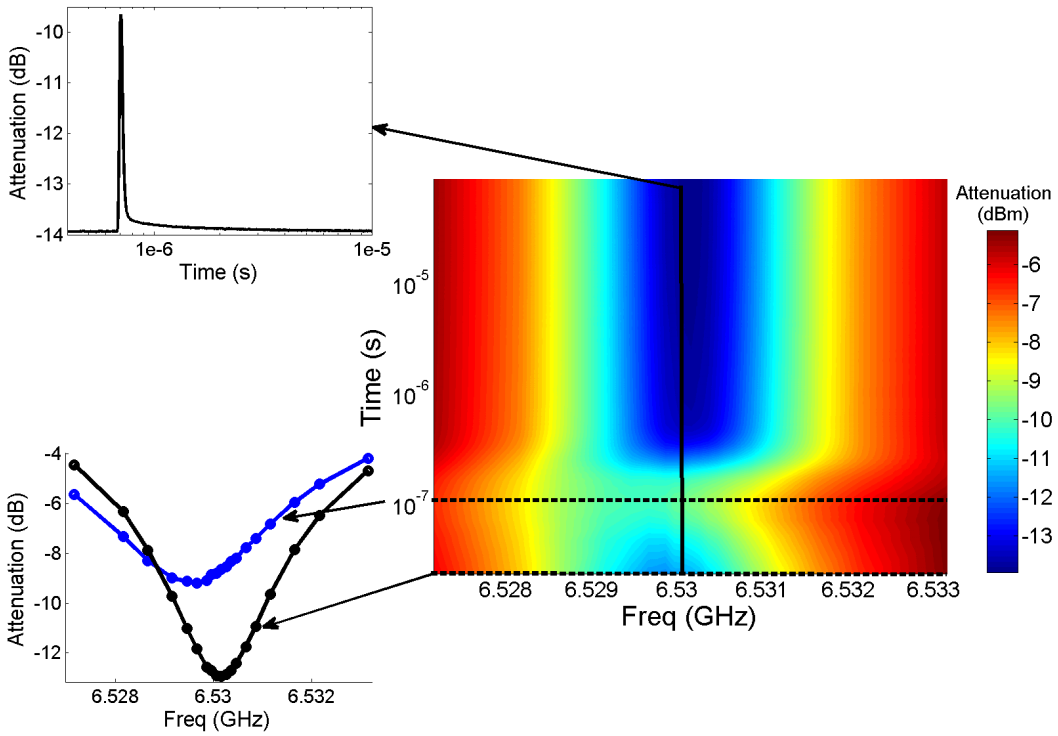

FIG. 7: Transient decay as a function of time and microwave frequency, with relevant cross-sections, taken at 530 nm.

After photoexcitation, the excess charge carriers not only modify the conductivity, they also modify the cavity resonance, with the largest shift occurring at the end of the laser pulse when the induced charge carrier density is maximum. Obtaining the pure decay of the conductivity, decoupled from the materials interaction with the temporally changing cavity resonance, requires careful data analysis.

Rather than comparing the conductivity at the fixed resonance frequency of the cavity f_0 (vertical arrow in Fig 8), the conductivity (at each point in time), should be compared at the time dependent resonance frequency $f_{res}(t)$ (diagonal arrow in Fig 8). The resonance frequency and resonant conductivity can then be calculated for each time point from the fit of the reconstructed resonance (see Fig. 7) .

	$\Delta\sigma$		$\Delta\sigma_{corr}$		Δf_{res}	
	530	780	530	780	530	780
μ_{fast}/μ_{slow}	14.83	15.44	12.23	12.24	17.88	22.63
τ_{fast} (μs)	0.109	0.116	0.111	0.1204	0.080	0.090
τ_{slow} (μs)	2.055	2.381	2.107	2.265	1.077	1.611
β	0.367	0.71	0.372	0.376	0.331	0.364

TABLE I: Comparison of polarization and conductivity decays taken in the high carrier density regime.

The polarization data was taken at high laser intensity ($10^{11} ph/cm^2$), and so the resonance frequency shift presented here is larger then that present in the spectrally resolved data set. We calculate the maximum difference between μ_{fast}/μ_{slow} taken with and without correcting for this resonance shift to be 5.5%. Since we did not perform this correction for the data presented

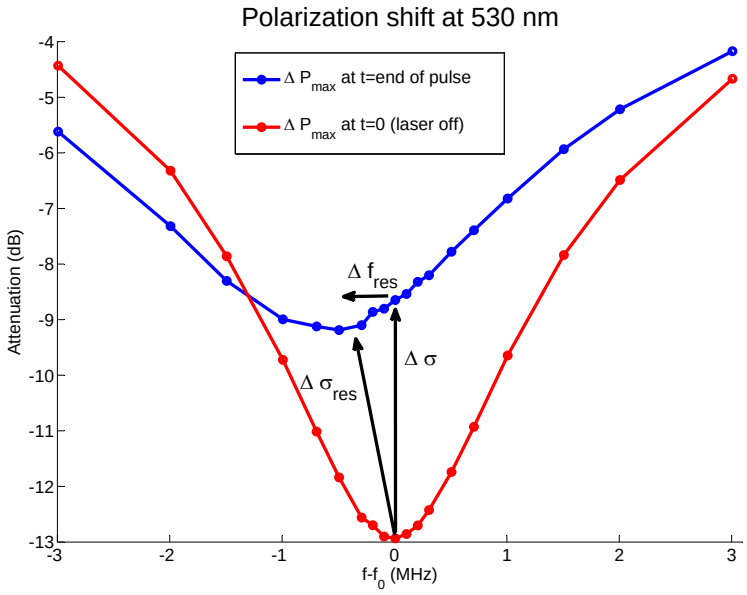

FIG. 8: Change in resonance power as a function of resonance frequency shift. Each point represents a point in time during the transient.

in the main text, we set the maximum error of μ_{fast}/μ_{slow} to be 5.5%.

Fig 9 shows the evolution of the resonance shift during the decay. We can see that the peak power shifts linearly with resonance frequency during photoexcitation, but follows a curved trajectory during the decay back to the dark resonance frequency. This is further evidence for decay via trapped states.

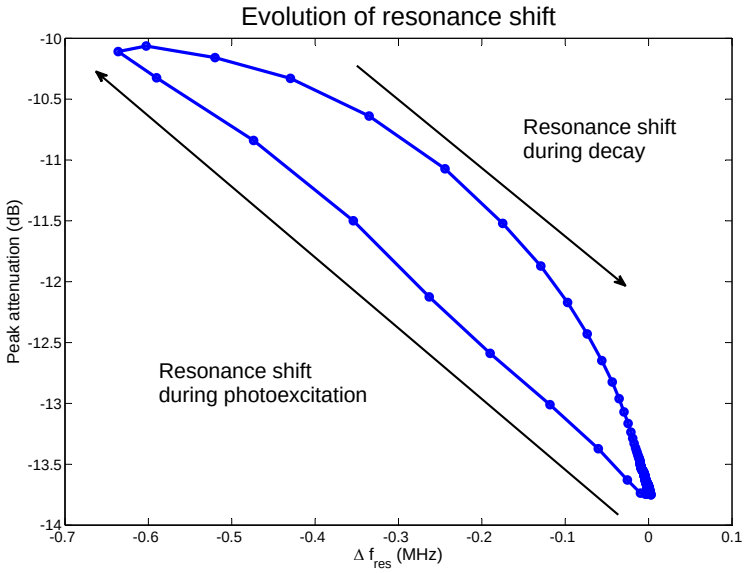

FIG. 9: change in resonance power as a function of resonance frequency shift. Each point represents a point in time during a the transient.

S5: DATA ANALYSIS DETAILS

TRMC is a technique which has been well explained elsewhere[3,4]. We measure the reflected power vs incident power.

$$y = \frac{P_r(t)}{P_i} \ [dBm] \tag{1}$$

However, photoinduced change in conductivity $\Delta\sigma$ is related to the *change* in reflected power.

$$\frac{\Delta P_r(t)}{P_r} = A\Delta\sigma, \tag{2}$$

where A (Ω cm) is the sensitivity factor of the cavity. We need to convert reflected power vs incident power to change in reflected power[5]. We do this by converting to a linear scale:

$$y' = 10^{y/10} \ [mW], \tag{3}$$

and then performing a background subtraction and rescaling:

$$\frac{\Delta P_r(t)}{P_r} = \frac{(P_r/P_i)^{\Delta\sigma} - (P_r/P_i)^0}{(P_r/P_i)^0} = \frac{y' - y'(0)}{y'(0)} \ [no\ units]. \tag{4}$$

Conductivity is related to charge carrier mobility μ_i ($\mathrm{cm^2V^{-1}s^{-1}}$) and carrier concentration N_i ($\mathrm{cm^{-2}}$) via

$$\sigma(t) = e\sum_i N_i(t)\mu_i. \tag{5}$$

Assuming no recombination of the initially formed charge carriers occurs during the laser pulse, the maximum (end-of-pulse) change in conductivity is given by

$$\Delta\sigma_{max} = eN_{max}\sum_i \mu_i = eI_0F_a(\lambda)\phi\sum_i \mu_i, \tag{6}$$

where e is the charge of an electron, I_0 is the photon intensity incident on the sample (photons/$\mathrm{cm^2}$) , $F_a(\lambda) = 1 - e^{-\alpha(\lambda)d}$ is the fraction of incident light absorbed at a given wavelength (assuming no reflection), and ϕ is the internal quantum efficiency.

The sensitivity factor of the cavity, A was determined using a phosphorus doped silicon calibration sample with known conductivity, doping concentration, reflection and absorption coefficients, thickness and internal quantum efficiency. Note: A acts as a scaling parameter for the transients, which means that errors in A only result in a shift in the absolute value of mobility, and cannot be responsible for the relative amplitudes of the TRMC peaks at different intensities.

In order to perform comparisons of the transients taken at different wavelengths and excitation intensities, we convert photoinduced conductivity changes (which depend on the number of carriers), to mobility per charge carrier:

$$\phi\sum\mu = \frac{1}{eI_0F_a(\lambda)}\ \frac{1}{A}\ \frac{\Delta P_r(t)}{P_r}. \tag{7}$$

S6 - FITTING TRMC TRANSIENTS.

We obtained TRMC transients at a range of excitation intensities, for wavelengths of 530, 650, 760, 780, 800 and 900 nm which span the above, inter and sub bandgap regime. Figure 10 shows conductivity transients taken using 530 and 780 nm excitation wavelengths at various intensities, fit with

$$y = Ae^{-t/\tau_f} + Be^{-(t/\tau_s)^\beta}. \tag{8}$$

In order to accurately fit the tail of the transient (which is 1-2 orders of magnitude smaller than the peak), it is useful to display traces in loglog format. Fits which appear accurate on a linear scale can be qualitiatvely incorrect for values close to zero. Another reason why data should be presented in loglog form is to compare the tail to the noise floor. We find that in the majority of previous TRMC literature (investigating lead-iodide perovskites as well as inorganic semiconductors), authors take traces on a timescale too short to accurately fit the long tail (1-5 μs are typical timescales for TRMC traces). This is because on a linear axis, it is difficult to see if the signal has decayed back to the noise floor or not. Fig 10 shows that even after 100 us, the decay tail has not reached the nosie floor of the instrument.

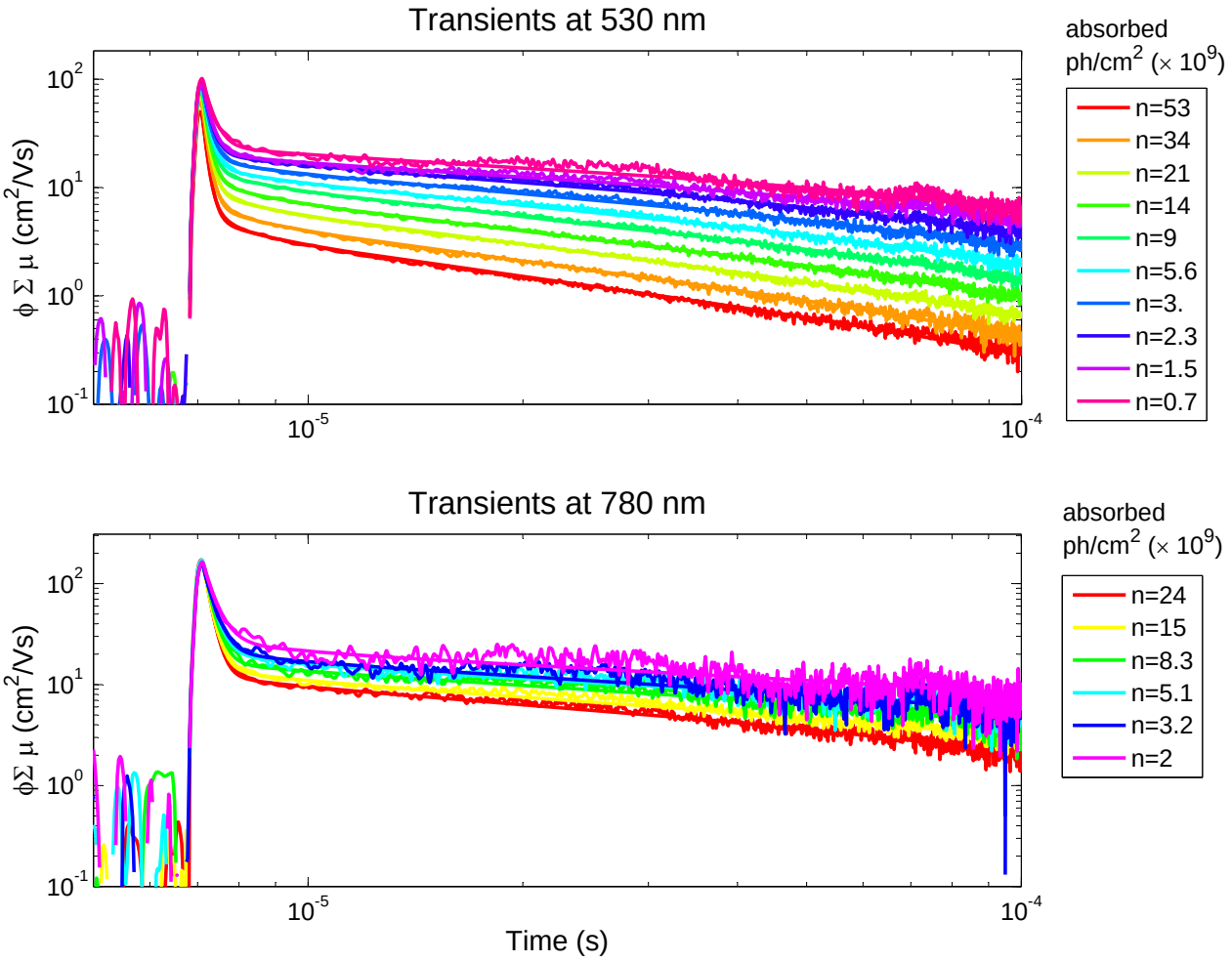

FIG. 10: TRMC transients with fits. Both plots have the same axes.

The feature which emerges at 20 and 80 μs at low excitation densities is a measurement artifact.

S7 - INTENSITY AND WAVELENGTH DEPENDENCE OF TRANSIENTS

The wavelength dependance of both the long decay time constant and the relative amplitude of the tail can be seen in Fig. 11, which shows normalized transients taken at fixed I_0 ($\approx 5 \times 10^9$ ph/cm^2) at various wavelengths.

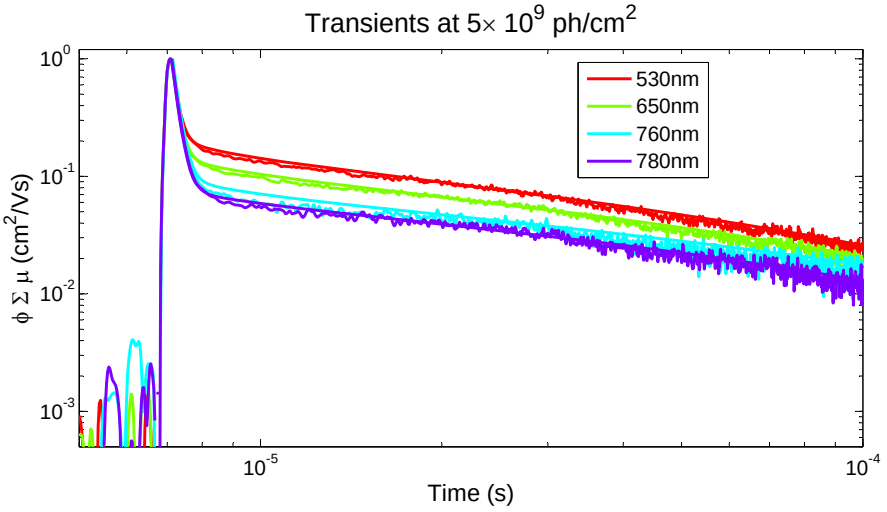

FIG. 11: Comparison of transients taken with different excitation wavelengths, for a fixed number of absorbed photons/cm^2

Figure 12 shows the maximum mobilities as a function of charge carrier density for wavelengths across the absorption spectrum of $CH_3NH_3PbI_3$. We note that previous TRMC studies have been performed only at wavelength above the bandgap (i.e. < 600 nm), and at charge carrier densities in the range $10^{10} - 10^{16}$, and at microwave frequencies above 9 GHz. Direct comparison of the obtained mobilities is not possible, however, we find that our data is qualitatively consistent with the results of Hutter[1],Oga[6] and Wojciechowski[7], but not with Ponseca[8].

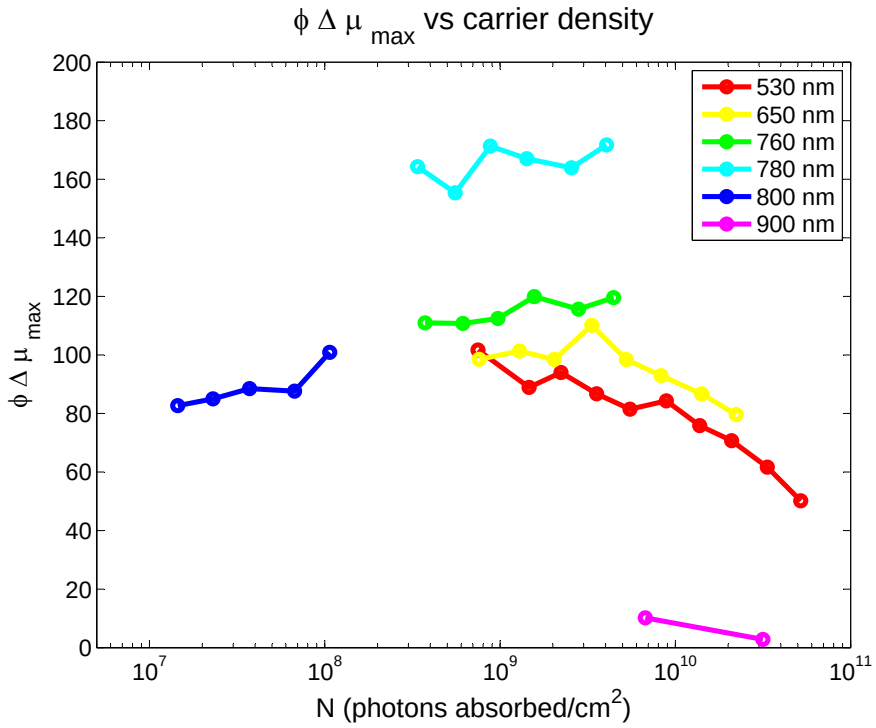

FIG. 12: Intensity dependence of maximum end of pulse mobility

Figure 13 shows the spectral dependance of the mobility (as well its slow and fast components) at various charge carrier densities. We note that the trends presented in the main text are consistant across two orders of magnitude in charge carrier density.

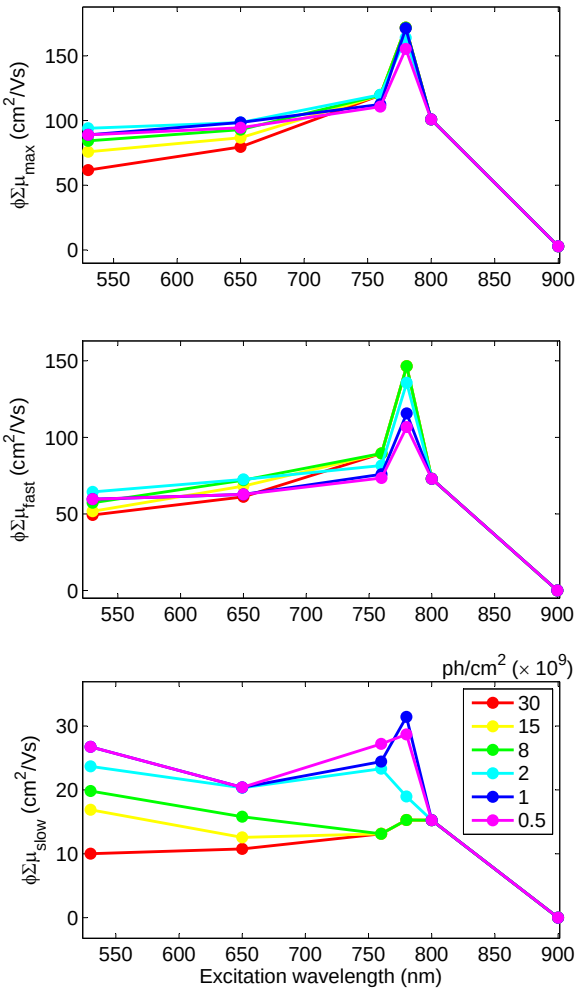

FIG. 13: Spectral dependence of the maximum end of pulse mobility (top), and it's decomposition into fast (middle) and slow (bottom) components at different excitation intensities. The legend is common for all plots.

* Electronic address: dane.mccamey@unsw.edu.au

[1] E. M. Hutter, G. E. Eperon, S. D. Stranks, and T. J. Savenije, The Journal of Physical Chemistry Letters **6**, 3082 (2015).
[2] F. Huang, Y. Dkhissi, W. Huang, M. Xiao, I. Benesperi, S. Rubanov, Y. Zhu, X. Lin, L. Jiang, Y. Zhou, A. Gray-Weale, J. Etheridge, C. R. McNeill, R. A. Caruso, U. Bach, L. Spiccia, and Y.-B. Cheng, Nano Energy **10**, 10 (2014).
[3] T. J. Savenije, A. J. Ferguson, N. Kopidakis, and G. Rumbles, The Journal of Physical Chemistry C **117**, 24085 (2013).
[4] a. Saeki, S. Seki, T. Sunagawa, K. Ushida, and S. Tagawa, Philosophical Magazine **86**, 1261 (2006).
[5] P. P. Infelta, M. P. de Haas, and J. M. Warman, Radiation Physics and Chemistry (1977) **10**, 353 (1977).
[6] H. Oga, A. Saeki, Y. Ogomi, S. Hayase, and S. Seki, Journal of the American Chemical Society **136**, 13818 (2014), http://dx.doi.org/10.1021/ja506936f .
[7] K. Wojciechowski, S. D. Stranks, A. Abate, G. Sadoughi, A. Sadhanala, N. Kopidakis, G. Rumbles, C.-Z. Li, R. H. Friend, A. K.-Y. Jen, and H. J. Snaith, ACS Nano **8**, 12701 (2014).
[8] C. S. Ponseca, T. J. Savenije, M. Abdellah, K. Zheng, A. Yartsev, T. Pascher, T. Harlang, P. Chabera, T. Pullerits, A. Stepanov, J. P. Wolf, and V. Sundstrom, Journal of the American Chemical Society **136**, 5189 (2014), http://dx.doi.org/10.1021/ja412583t .